NOTES AND CORRESPONDENCE

A Modified Kain–Fritsch Scheme and Its Application for the Simulation of an Extreme Precipitation Event in Vietnam

NGUYEN MINH TRUONG AND TRAN TAN TIEN

Laboratory for Weather and Climate Forecasting, Hanoi University of Science, Hanoi, Vietnam

ROGER A. PIELKE SR.

Cooperative Institute for Research in Environmental Sciences, University of Colorado, Boulder, Colorado

CHRISTOPHER L. CASTRO

Department of Atmospheric Sciences, The University of Arizona, Tucson, Arizona

GIOVANNI LEONCINI

Meteorology Department, University of Reading, Reading, United Kingdom

ABSTRACT

From 24 to 26 November 2004, an extreme heavy rainfall event occurred in the mountainous provinces of central Vietnam, resulting in severe flooding along local rivers. The Regional Atmospheric Modeling System, version 4.4, is used to simulate this event. In the present study, the convective parameterization scheme includes the original Kain–Fritsch scheme and a modified one in which a new diagnostic equation to compute updraft velocity, closure assumption, and trigger function are developed. These modifications take the vertical gradient of the Exner function perturbation into account, with an on–off coefficient to account for the role of the advective terms. According to the event simulations, the simulated precipitation shows that the modified scheme with the new trigger function gives much better results than the original one. Moreover, the interaction between convection and the larger-scale environment is much stronger near the midtroposphere where the return flow associated with lower-level winter monsoon originates. As a result, the modified scheme produces larger and deeper stratiform clouds and leads to a significant amount of resolvable precipitation. On the contrary, the resolvable precipitation is small when the original scheme is used. The improvement in the simulated precipitation is caused by a more explicit physical mechanism of the new trigger function and suggests that the trigger function needs to be developed along with other components of the scheme, such as closure assumption and cloud model, as a whole. The formalistic inclusion of the advective terms in the new equation gives almost no additional improvement of the simulated precipitation.

1. Introduction

Central Vietnam is a narrow region lying along the South China Sea between 10.5° and 20°N where the local weather is frequently affected by tropical circula-

tions that originate offshore. Because the region is mountainous with a narrow coastal plain the rivers are remarkably steep. Severe flooding events tend to occur in boreal fall with the seasonal passage of the ITCZ. Specific recent events include 18–20 September 2002 in the Nghe An and Ha Tinh provinces, 10–13 November 2003 in the Binh Dinh and Phu Yen provinces, and 24–26 November 2004 in Hue and Quang Nam provinces. These events caused damage to infrastructure and property and, in the September 2002 case, caused

hundreds of injuries and deaths. Significant deforestation in the mountainous regions upstream of the rivers has likely exacerbated the flood risk in recent decades. The socioeconomic impact of such events motivates studies with numerical weather prediction (NWP) models to improve operational forecasting of heavy rainfall events. If the models are found to have skill, they could be used as input data for hydrological models to predict the specific geographic locations that may experience a flood.

In recent decades there have been many studies related to convective weather and improvement of rainfall forecasts that have provided a better understanding of physical and dynamical processes. For example, studies on cloud microphysics focus on the parameterization of mass and energy conservation between water substances and are applied to cloud models for different weather situations (Lin et al. 1983; Rutledge and Hobbs 1984). There has been remarkable success in meso-γ-scale research (e.g., Klemp and Wilhelmson 1978a,b; Finley et al. 2001; Cai and Wakimoto 2001), which showed the characterization of the dynamic structure, including the distribution of the pressure perturbation gradient, which affects the evolution and movement of thunderstorms as well as their influence on local weather.

Meso-γ orographic effects on the dynamic structure of airflow over mountains have also been well documented. Recently, Doyle and Durran (2002) depicted the formation of low-level rotors, horizontal vorticity, and waves propagating to upper levels caused by a 600-m-high mountain. The above and many other studies have directly or indirectly depicted the presence of a pressure perturbation, which may be closely associated with flow and precipitation regimes over complex terrain (Chu and Lin 2000; Chen and Lin 2005).

For the meso-β or larger scale, research has concentrated on the development of conceptual cloud models for modeling the entrainment–detrainment rate at cloud lateral boundaries and properties of updrafts and downdrafts (Frank and Cohen 1985; Raymond and Blyth 1986; Kain and Fritsch 1990; Mapes 2000; Xu and Randall 2001). Also several convective parameterization schemes (CPS) applicable to various types of numerical models have been developed (Arakawa and Schubert 1974; Kuo 1974; Fritsch and Chappell 1980; Tiedtke 1989) and chosen for particular atmospheric circulations or numerical models (Grell and Kuo 1991; Cohen 2002).

Observations may improve the physical understanding of dynamical processes in convective systems. These may be useful for diagnostic and numerical studies (Yanai and Johnson 1993; Xu and Randall 2001). In particular, nonhydrostatic pressure might play an important role in convective systems (Xu and Randall 2001). However, that is not accounted for in the current version of the Kain–Fritsch (KF) CPS (Kain 2004; Kain and Fritsch 1993) used in the operational version of the Eta model in North America. Consequently, here our purpose is to find out how to analytically account for nonhydrostatic pressure, or the Exner function perturbation, in the CPS and determine if its presence significantly improves the simulated precipitation. In section 2 of this study, a brief description of the original KF CPS and modifications to it are given. The model setup for event simulations is described in section 3 and the event simulation results of the 24–26 November 2004 flood event are described in section 4. A summary is given in section 5. The Regional Atmospheric Modeling System (RAMS), version 4.4, is used in this study. Its comprehensive description can be found in Pielke et al. (1992) and Cotton et al. (2003). [The RAMS user's guide is also available online from the Atmospheric, Meteorological, and Environmental Technologies (ATMET) Corporation at www.atmet.com.]

2. The original KF CPS and modifications

a. The original KF CPS

The KF CPS contains five key components including the trigger function, moist convective updraft, moist convective downdraft, compensating circulation, and closure assumption, which are outlined below [for more details and formulas refer to Kain and Fritsch (1990, 1993), Kain et al. (2003), Kain (2004), and Castro (2005)].

1) TRIGGER FUNCTION

As a decisive factor to initiate convection in mesoscale models, the trigger function is presumably as important as CPS since it decides when and where deep convection should occur (Rogers and Fritsch 1996; Hong and Pan 1998; Kain 2004). The Kain (2004) procedure to determine the trigger function is implemented as following.

Beginning at the surface, updraft source layers (USLs) are determined to include vertically adjacent model layers whose total depth is at least 50 hPa. The parcel's thermodynamic properties are mass weighted.

The parcel is lifted to its lifting condensation level (LCL). A temperature perturbation (ΔT) is added to its temperature at the LCL (T_{LCL}). A check is done to see if convection initiates

$$\begin{cases} T_{LCL} + \Delta T > T_{ENV}, & \text{convection initiates} \\ \text{Search for another potential USL,} & \text{otherwise,} \end{cases}$$

(1)

where T_{ENV} is the environment temperature at the LCL. The temperature perturbation is a function of the running mean of the grid-scale vertical velocity and the LCL height above the ground (Z_{LCL}, m). If convection initiates the initial vertical velocity of the parcel (w_{LCL}) is given by

$$w_{LCL} = 1 + 1.1[(Z_{LCL} - Z_{USL})\Delta T / T_{ENV}]^{1/2}, \quad (2)$$

where Z_{USL} is the height of the USL base. Here w_{LCL} is then used as the lower boundary value for the equation to compute updraft velocity.

2) MOIST CONVECTIVE UPDRAFT

In the original KF CPS, the updraft component executes the following steps:

- Updraft mass flux at the LCL is computed using the updraft radius given by Kain (2004). The component loops from the LCL to the cloud top to compute the updraft mass flux, updraft entrainment and detrainment rates, liquid and ice phases of water, and precipitation generated at each level.
- Within the loop, the component checks if the parcel is supersaturated, then the condensate is computed. Otherwise, appropriate adjustments to the parcel temperature, water vapor, and liquid and ice mixing ratios are made. A check is also made to see if the temperature is less than 248.16 K, then all liquid water is frozen. The new thermodynamic properties of the column due to the effects of freezing are calculated.
- As the next step, the component computes precipitation generated within the updraft, along with liquid (qout$_{liq}$) and solid precipitation (qout$_{sol}$) generated at the given model level as a function of the updraft velocity. The effect of drag (P_{drag}) from the liquid and solid water substances is determined and put into the updraft velocity equation:

$$\frac{1}{2}\frac{dw_u^2}{dz} = \frac{g}{1 + 0.5}\left(\frac{T_u - \overline{T}}{\overline{T}}\right) - \text{Ent} - P_{drag}, \quad (3)$$

where w and T are the vertical velocity and virtual absolute temperature, respectively; the subscript "u" denotes the updraft variables; and the overbar denotes the grid-scale variables. Ent denotes entrainment. In Eq. (3) the coefficient 0.5 is added to account for the virtual mass effect that compensates for nonhydrostatic pressure perturbations (Anthes 1977; Donner 1993). Then, the updated values of liquid and ice water mixing ratios are determined as a function

of the updraft velocity. If w_u is less than zero, cloud top (CT) is defined at this point.

- The updraft entrainment and detrainment rates are computed. The updraft mass flux (UMF) at the given model level is a function of the updraft mass flux at the lower model level and detrainment and entrainment. The final updated water vapor mixing ratio, liquid water mixing ratio, and ice mixing ratios are computed. The precipitation (P) generated at the given model level is

$$P = \text{qout}_{liq}\text{UMF} + \text{qout}_{sol}\text{UMF}. \quad (4)$$

The total updraft-generated precipitation is calculated as the sum of precipitation generated at each model level.

3) MOIST CONVECTIVE DOWNDRAFT

The downdraft component implements the steps below:

- Precipitation efficiency (Peff) is defined to be a function of wind shear and height of cloud base. The level of free sinking (LFS) at which the downdraft starts is assumed to be at least 150 mb above the cloud base. Downdraft thermodynamic properties at the LFS are computed. The initial downdraft mass flux (DMF) at the LFS is computed as a function of Peff.
- The downdraft entrainment rate is a function of DMF$_{LFS}$ and changes linearly with pressure between LFS and LCL. Downdraft properties are adjusted to account for entrainment.
- If the USL base of the updraft parcel is below the melting level, then all solid phase precipitation in the column is melted and new thermodynamic properties of the downdraft at the LCL are computed. From the LCL to the surface, relative humidity reduces 20% (1 km)$^{-1}$. If the downdraft virtual temperature exceeds that of the environment, the parcel is neutrally buoyant and that level is where the downdraft stops sinking. Otherwise, it reaches the surface.
- When the downdraft enters the USL, entrainment stops and detrainment starts. Detrainment is a function of DMF$_{LFS}$ and changes linearly with pressure between LFS and the level of downdraft neutral buoyancy or the surface.
- The downdraft parcel evaporates water on its decent from the LCL. At each model level this evaporated water (EVAP) is determined. Ultimately, the net generated precipitation (P_{net}) is computed by

$$P_{net} = P - \text{EVAP}. \quad (5)$$

4) COMPENSATING CIRCULATION

After updraft and downdraft fluxes are determined, the scheme computes compensating mass flux so that the net vertical mass flux at any level is zero. The compensating mass flux is equal to the sum of entrainment and detrainment caused by updraft and downdraft. Compensating terms for thermodynamic properties are computed at a given model level, depending if the compensating mass flux is positive or negative. Hydrometeors are redistributed in the same manner, and this component feeds back the detrained values of liquid and solid water to RAMS. Thus, accuracy in computing updraft velocity might affect not only cloud depth, generated precipitation, and downdraft, but thermodynamic properties of the compensating circulation and resolvable precipitation also.

5) CLOSURE ASSUMPTION

In the original KF CPS the closure assumption is to remove (at least 90% of) CAPE over the convective time scale (30 min–1 h), which is defined as

$$\text{CAPE} = \int_{\text{LCL}}^{\text{CT}} g \frac{T_u(z) - \overline{T}(z)}{\overline{T}(z)} dz. \qquad (6)$$

If the closure assumption is not met, the scheme incrementally increases mass fluxes following the algorithm described by Castro (2005).

b. Modifications

The modifications to the KF CPS are motivated by three reasons. 1) The diagnostic study by Xu and Randall (2001) demonstrates that the effect caused by the vertical gradient of pressure perturbation may be important. However, as seen in section 2a, an explicit treatment of this effect is omitted in all components of the original scheme. 2) In the original trigger function, the convective inhibition (CIN) from the USL top to the LCL is not explicitly taken into account, although it might be large according to Rogers and Fritsch (1996). 3) Equations and expressions describing convective parameterization schemes need to have a relationship as close as possible to the dynamic core of numerical models in which they are incorporated.

Mathematically, if we can analytically compute the

ratio between the vertical gradient of the Exner function perturbation (equivalent to pressure perturbation) and buoyant force (PDB, see the appendix) for the updrafts, using RAMS third equation of motion, we can also derive a new diagnostic equation to compute the updraft velocity, closure assumption, and trigger function in the KF CPS as below.

Assuming that PDB is applicable when using the parcel theory, in the present study the equation for the updraft velocity is written as

$$\frac{1}{2} \frac{dw_u^2}{dz} = g \left(\frac{T_u - \overline{T}}{\overline{T}} \right) (1 + \text{PDB}) - \text{Ent} - P_{\text{drag}}. \qquad (7)$$

To be consistent with Eq. (7), in the present study CAPE is redefined as

$$\text{CAPE} = \int_{\text{LCL}}^{\text{CT}} g \frac{T_u(z) - \overline{T}(z)}{\overline{T}(z)} [1 + \text{PDB}(z)] dz \qquad (8)$$

and used for the closure assumption. With the definition in (8), deep convections can be maintained with negative buoyancy provided that the vertical gradient of pressure perturbation is positive and large enough.

For the trigger function, Rogers and Fritsch (1996) proposed a framework for the trigger function applicable to a wide variety of environments. Unfortunately, because of the lack of theoretical or empirical formulations they had to impose parameters in their own trigger function. A similarity may be found in Hong and Pan (1998).

In the present study, a new trigger function is proposed and tested against the original one. First, we define a function containing the two terms on the right-hand side of Eq. (8):

$$\text{Ftri} = g \frac{T_u(z) - \overline{T}(z)}{\overline{T}(z)} [1 + \text{PDB}(z)], \qquad (9)$$

where T_u follows dry adiabatic curve under the LCL and its lower boundary value is assumed equal to the environment temperature at the USL base plus the temperature perturbation as in Eq. (1). Then the trigger function is defined by the contemporaneous verification of the following conditions:

$$\begin{cases} \begin{cases} \text{Ftri}_{\text{USL}} > 0 \\ w_{\text{MIX}}^2 + 2(\text{Ftri}_{\text{USL}} + \text{Ftri}_{\text{USL-LCL}}) > 0, \ w_{\text{MIX}} > 0, \quad \text{convection initiates} \\ -w_{\text{MIX}}^2 + 2(\text{Ftri}_{\text{USL}} + \text{Ftri}_{\text{USL-LCL}}) > 0, \ w_{\text{MIX}} < 0 \end{cases} \\ \text{Search for another potential USL, otherwise,} \end{cases} \qquad (10)$$

where Ftri$_{USL}$ and Ftri$_{USL-LCL}$ are the integration of the Ftri in the USL and from the USL top to the LCL, respectively; and w_{MIX} is the mass-weighted vertical velocity within the USL. The first assumption supposes that forcings within the USL can support upward parcels. The second assumes that although the updraft parcels have upward velocity the environment beneath the LCL must still have conditions favorable enough for

them to reach the LCL, and the third, if updraft parcels have downward velocity then the environment must have strong conditions for them to penetrate the layer from the USL top to LCL. Similar to the original KF CPS the check for USLs is carried out at every grid point in the lowest 300 hPa of the atmosphere. In case convection initiates, the initial updraft velocity at the LCL is simply computed by

$$
w_{LCL} = \begin{cases} \left\{ w_{MIX}^2 + 2\int_{USLbase}^{LCL} g\dfrac{T_u(z) - \overline{T}(z)}{\overline{T}(z)}[1 + \text{PDB}(z)]\,dz \right\}^{1/2}, & w_{MIX} > 0 \\[3ex] \left\{ -w_{MIX}^2 + 2\int_{USLbase}^{LCL} g\dfrac{T_u(z) - \overline{T}(z)}{\overline{T}(z)}[1 + \text{PDB}(z)]\,dz \right\}^{1/2}, & w_{MIX} < 0. \end{cases} \tag{11}
$$

3. Model configuration for event simulations

In section 2, the original KF CPS and scheme modifications are described. As the next step, in this section, numerical experiments are designed for event simulations to determine if scheme modifications can improve the total accumulative simulated rainfall (TASR) by comparing them to observed data.

The initial conditions for the RAMS simulations are created using the National Centers for Environmental Prediction–National Center for Atmospheric Research (NCEP–NCAR) reanalysis data (Kalnay et al. 1996) for the days of the flood event. These data consist of horizontal wind, temperature, relative humidity, and geopotential height on 17 isobaric surfaces with a horizontal resolution of 2.5° × 2.5°. The boundary conditions are updated every 6 h. A Barnes objective analysis scheme is used to interpolate the initial data onto the model grids. The interpolation operator for the updated lateral boundaries on the outer grid and boundary region between the coarse and nested grid is implemented using a quadratic function. The inner grid uses a two-way interactive nesting technique. Sea surface temperature used in the present study is weekly sea surface temperature given by the National Oceanic and Atmospheric Administration (NOAA; Reynolds et al. 2002).

The domain and the two grids used for the simulations are shown in Fig. 1a. Several experiments have been carried out (see Table 1 for the details) utilizing two grids, having horizontal grid spacings of 40 and 10 km, respectively. The KF CPS is switched on for both grids. As shown in Table 1, the trigger function (TF), closure assumption (CA), and equation to compute updraft velocity (UE), are optional. The experiments whose names carry the suffix "-tri" have been performed using the modified KF CPS with the new trigger

function, whereas "-cue" indicates that the modified KF CPS has been used with the new equation and closure assumption. Meanwhile, "-all" indicates all modifications, and "-ori" indicates the original scheme.

An explicit microphysical representation of resolvable precipitation is used for all simulations (Walko et al. 1995). The model grid has 30 levels and is vertically stretched with a 1.15 ratio. The lowest grid spacing is 100 m and the maximum vertical grid spacing is set to 1200 m. The highest level is about 23 km (30 mb).

4. Event simulations and discussions

a. Synoptic pattern and observed data

At 0000 UTC [0700 local time (LT)] 24 November 2004, Typhoon Muifa at its decaying stage was moving west toward southern Vietnam, more than hundred kilometers east of the coast. At the same time, an Asian continental cold high was moving south toward northern Vietnam. The combination of these synoptic features led to a strong convergent zone of the horizontal wind in central Vietnam where upward motion is expectedly large. Figure 1b shows the wind field at 1000 mb and sea level pressure, representing the synoptic pattern at this time. Afterward, the cyclone circulation was almost completely decayed (Figs. 2a,b), leaving a cold ridge over the north of Vietnam, which was continuously maintained on the second day. Using the modified KF CPS with all modifications, RAMS well reproduced the synoptic patterns at the corresponding times (Figs. 2c,d). Similar results could be given if the original KF CPS was used (not shown). The Truong Son Mountains, as shown in the depiction of the topography in Fig. 3, have an average height of about 1200–1500 m above mean sea level (MSL) and are located 50–120 km inland parallel to the coast. The mountains enhanced the convergence because their orientation is
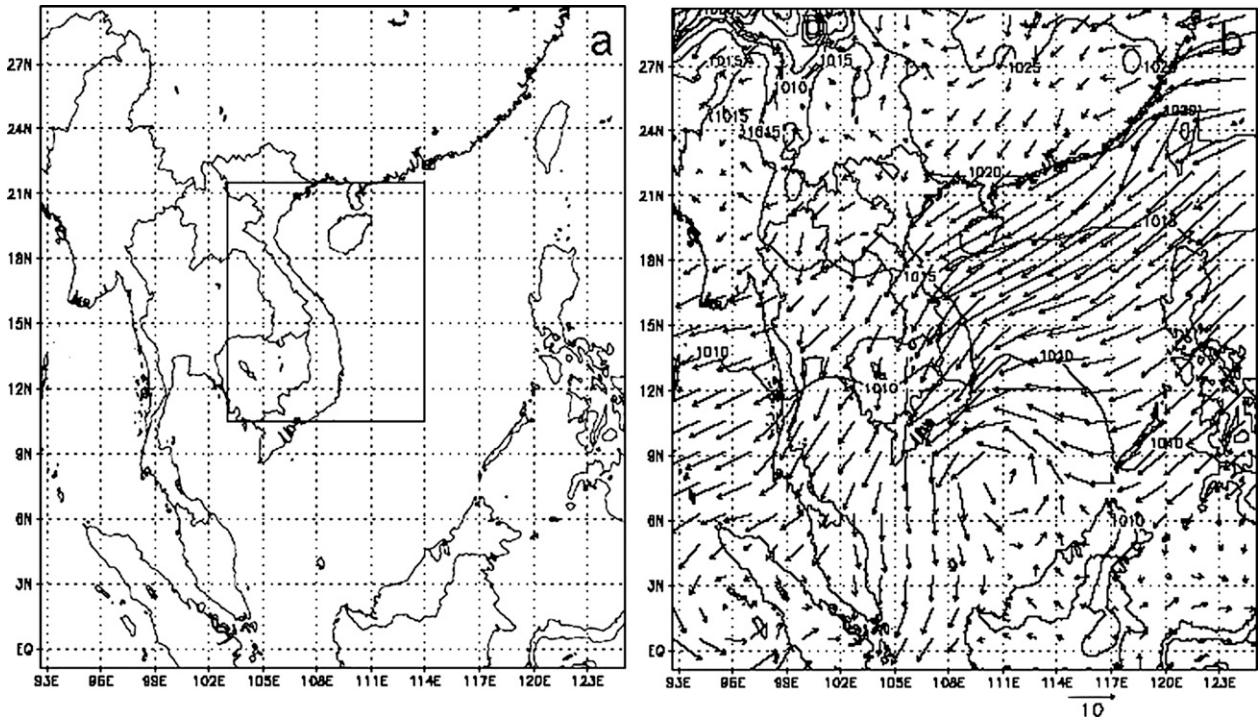
FIG. 1. (a) Grid configuration of the present study. (b) Sea level pressure and wind field over Vietnam and the South China Sea region at 1000 mb at 0000 UTC 24 Nov 2004.

roughly perpendicular to the synoptic-scale wind, producing strong topographically forced convection on their windward side. Besides, Bach Ma Mountain runs normal to the coastline and becomes a natural barrier to cold air masses, which makes cold fronts become stationary, producing large amounts of stratiform precipitation. Such meteorological conditions in central Vietnam generally occur in the transition seasons of fall and spring.

Visible satellite images show that by 1125 UTC 24 November 2004, a band of topographically forced convective clouds occurred north of 15°N in the Truong Son Mountains (Fig. 4a). During the second half of the day, a mesoscale convective complex developed on the mountains and propagated northward toward the coast (Fig. 4b). On the next day, the mesoscale convective complex dissipated, leaving a cirrus cloud curtain (Figs. 4c,d). This weather event produced heavy rainfall over

central Vietnam mainly during the first part of the period, causing severe floods. Six surface stations recorded a 48-h accumulative observed rainfall (AOR) above 500 mm, including Hue (656 mm), A Luoi (544 mm), Nam Dong (720 mm), Thuong Nhat (721 mm), Hiep Duc (584 mm), and Son Giang station (520 mm), which are numbered in Fig. 3 except Nam Dong located so close to Thuong Nhat station that it is not numbered. Among those stations, the former four are located in the north of Bach Ma Mountain, which creates a large concave topography normal to northeast direction. There were 22 additional stations in the area where 48-h AOR exceeded 200 mm. The present study uses the observed rainfall data given by the 205 sites shown in Fig. 3, all of which are on the windward side of the mountain range, including some island sites off the coast. The objectively analyzed AOR is shown in Fig. 5 where numbers are the absolute maxima measured at

TABLE 1. Event numerical experiments where TF, CA, and UE denote options for the trigger function, closure assumption, and equation to compute updraft velocity.

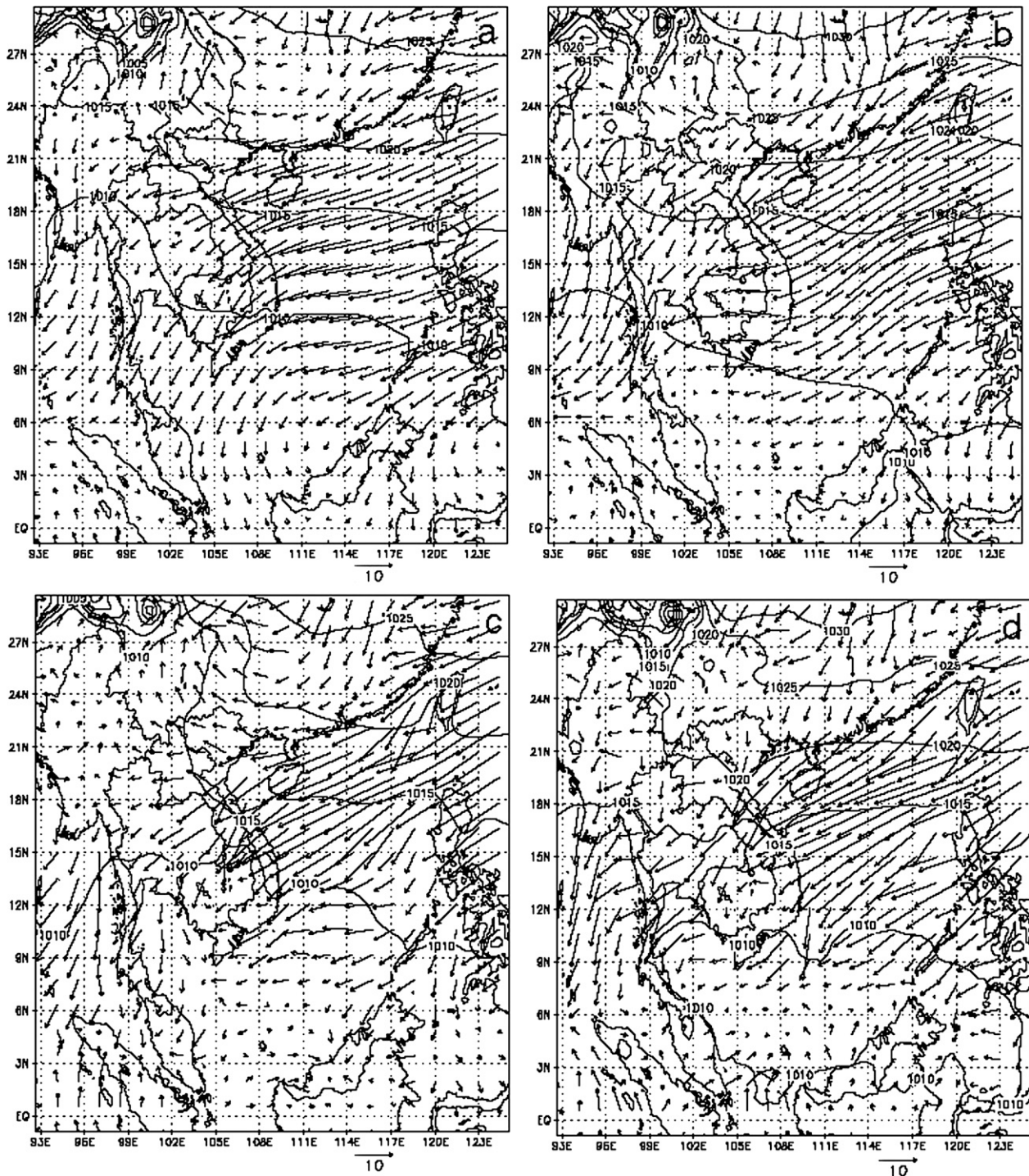| Case	TF	CA	UE	Grid domain (for all cases)	Grid center (for all cases)
I-ori	Original	Original	Original		
I-tri	Modified	Original	Original	1: 94 × 90	1: 15°N, 109°E
I-cue	Original	Modified	Modified	2: 122 × 126	2: 16.25°N, 108.5°E
I-all	Modified	Modified	Modified		

FIG. 2. As in Fig. 1b, but at (a) 1200 UTC 24 Nov and (b) 0000 UTC 25 Nov 2004. Simulations are given by RAMS at (c) 1200 UTC 24 Nov and (d) 0000 UTC 25 Nov 2004, using all modifications.

Thuong Nhat station (16.12°N, 107.68°E). Most of the AOR occurs on 24 November. There is a clear northward expansion of the heavy rainfall band, which is consistent with the propagation of the mesoscale convective complex.

In addition to gauge data, Fig. 6 presents data given by the Tropical Rainfall Measuring Mission (TRMM-3B42). The TRMM data give rainfall rates with 3-h resolution at 0000 (r1), 0300 (r2), 0600 (r3), 0900 (r4), 1200 UTC (r5), and so on, then for example, 12-h accu-
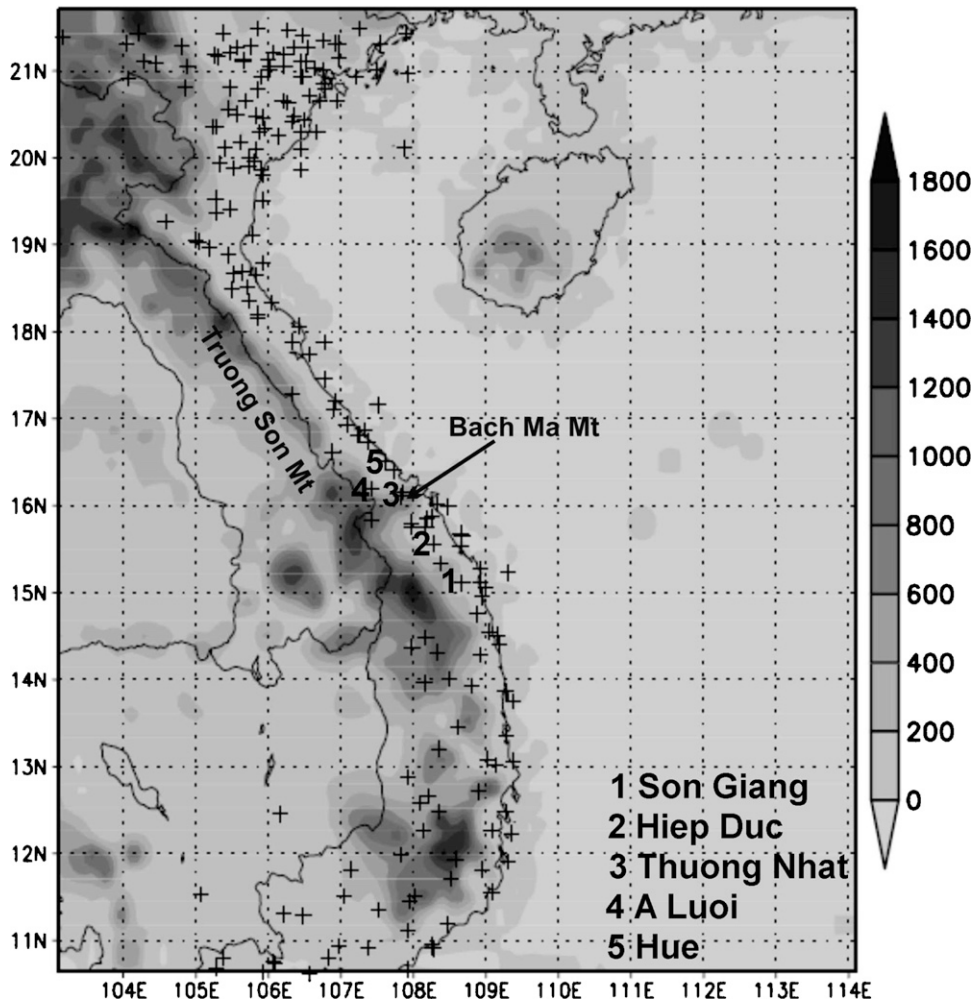
FIG. 3. Grid 2 topography (shaded; m MSL). Symbols are the observation sites. Numbers are stations where 48-h accumulative observed rainfall exceeds 500 mm.

mulative rainfall is computed by 3[(r1 + r5)/2 + r2 + r3 + r4]. The 24-, 36-, and 48-h accumulative rainfalls are computed in the same way. Basically, the TRMM data are consistent with the gauge data and satellite images except for two things: first, they do not give the local maximum at Hiep Duc station (15.58°N, 108.12°E); and second, their maxima on the first day are noticeably smaller than the gauge data, although their 48-h absolute maximum comes to 713 mm. However, they can complement where the gauge data are absent, for example, over the seas. As a result, the TRMM data assert that the heavy rainfall band is located on land.

b. Total simulated rainfall

For case I-ori (original KF CPS), the 48-h TASR for grid 2 is given in Fig. 7a. The spatial distribution of the

rainfall shows an acceptable comparison with the visible satellite cloud images on those days (Fig. 4). The northward expansion of the heavy rainfall region is captured (to be brief, the 12-, 24-, and 36-h TASR are not shown). However, this model simulation drastically underestimates the rainfall (Table 2). The maximum 48-h TASR is only 345 mm and the corresponding AOR is over 2 times that amount at 721 mm. A comparison with Figs. 5 and 6 shows that the simulated rainfall region in the southwest corner of the domain seems unreasonable. For operational purposes, the significant underestimation of the simulated heavy rainfall region would provide an incorrect flood warning for this event.

To realize the role of the trigger function, the modified KF CPS with the new trigger function is applied. For case I-tri, the 48-h TASR is shown in Fig. 7b. Simi-
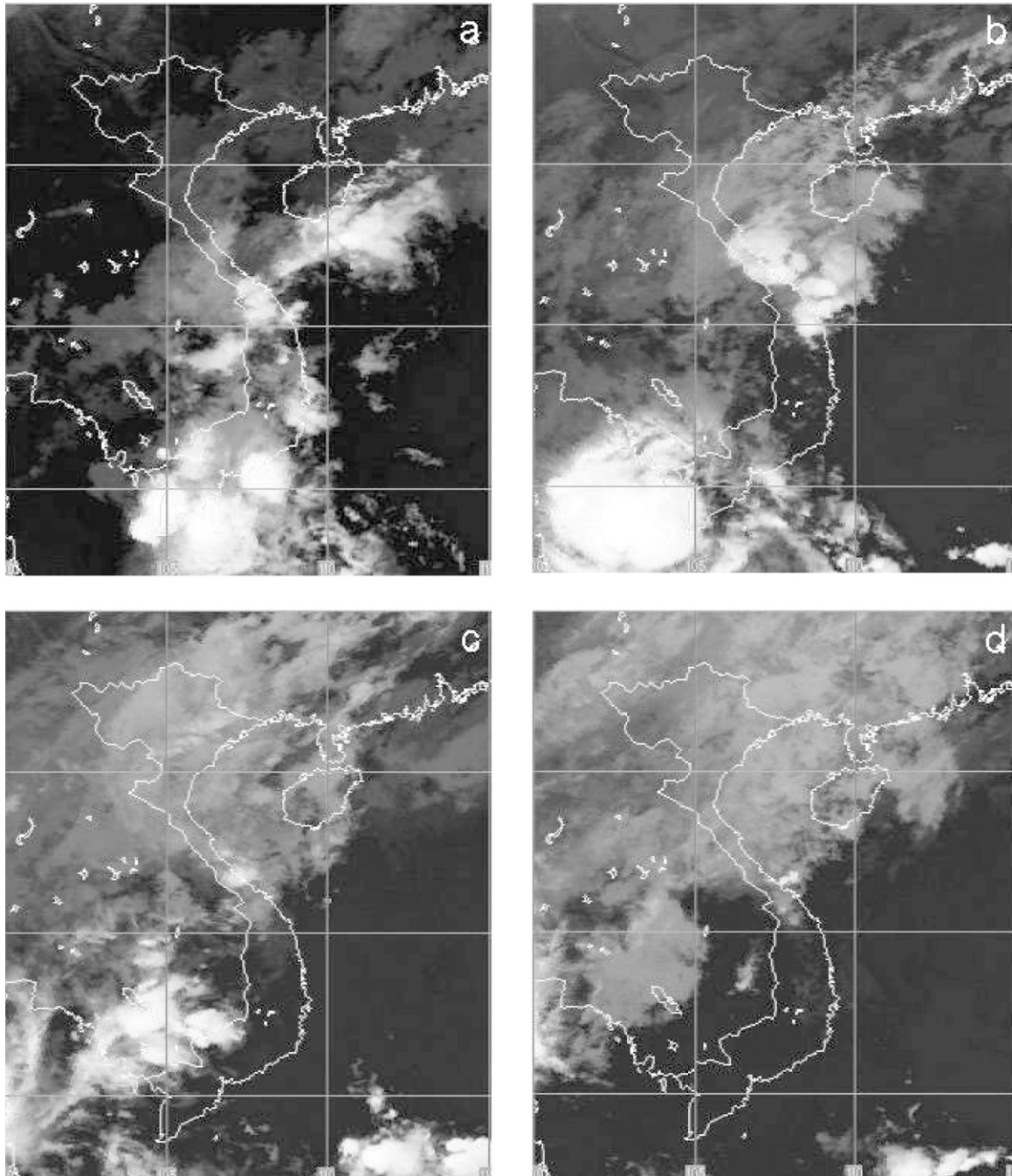
Fig. 4. Visible satellite images at (a) 1125 UTC 24 Nov, (b) 2325 UTC 24 Nov, (c) 1125 UTC 25 Nov, and (d) 2325 UTC 25 Nov 2004.

lar to case I-ori, simulation I-tri also underestimates the rainfall (Table 2). However, the maximum 48-h TASR increases to 493 mm, about 150 mm larger than case I-ori. Besides, the simulated rainfall region in the southwest corner disappears and the local maximum center near Thuong Nhat station (16.12°N, 107.68°E) is more clearly simulated. Nevertheless, case I-tri cannot well

capture the northward expansion of the heavy rainfall region as case I-ori does (the 12-, 24-, and 36-h TASR are not shown).

For case I-cue, the modified KF CPS with the original trigger function, the maximum 48-h TASR is almost the same as case I-ori (Fig. 7c), although it comes to 138 mm after the 12-h integration (Table 2). Similar to case
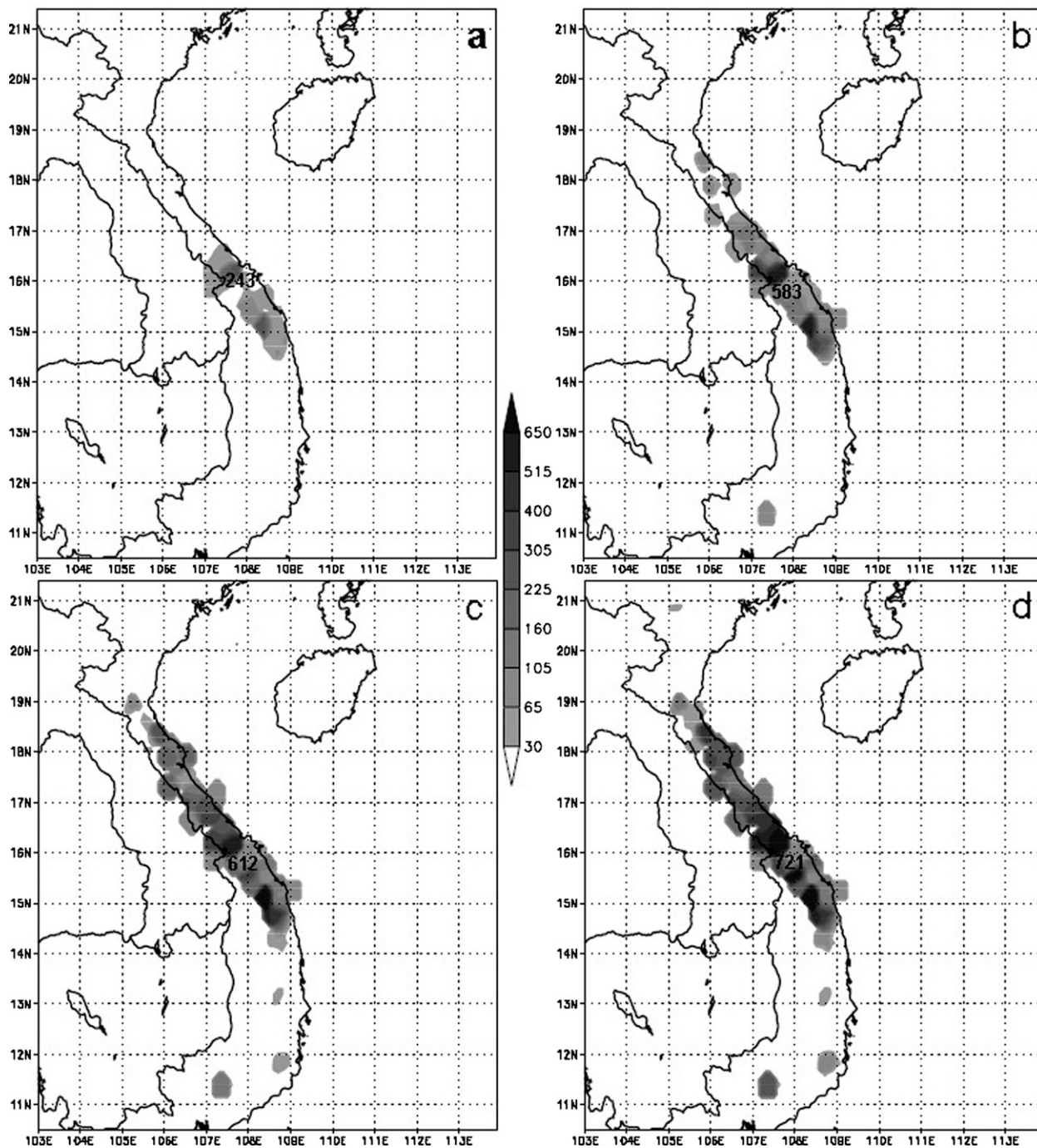
FIG. 5. Objective analyses of the observed precipitation (mm), accumulated for (a) 12, (b) 24, (c) 36, and (d) 48 h, starting from 0000 UTC 24 Nov 2004. Numbers are the absolute maxima measured at Thuong Nhat (16.12°N, 107.68°E).

I-ori, the simulated rainfall region in the southwest corner is found, but the northward expansion of the heavy rainfall region is not depicted, and the local maximum center near Thuong Nhat station (16.12°N, 107.68°E) is not clearly reproduced (the 12-, 24-, and 36-h TASR are not shown). At this point of view so far, the original

trigger function appears "more strict" than the new one in producing maximum TASRs. On the contrary, convection seems to initiate less frequently using the new equation to compute updraft velocity and closure assumption. A more interesting thing is that the heavy rainfall band location is not uniquely decided by the
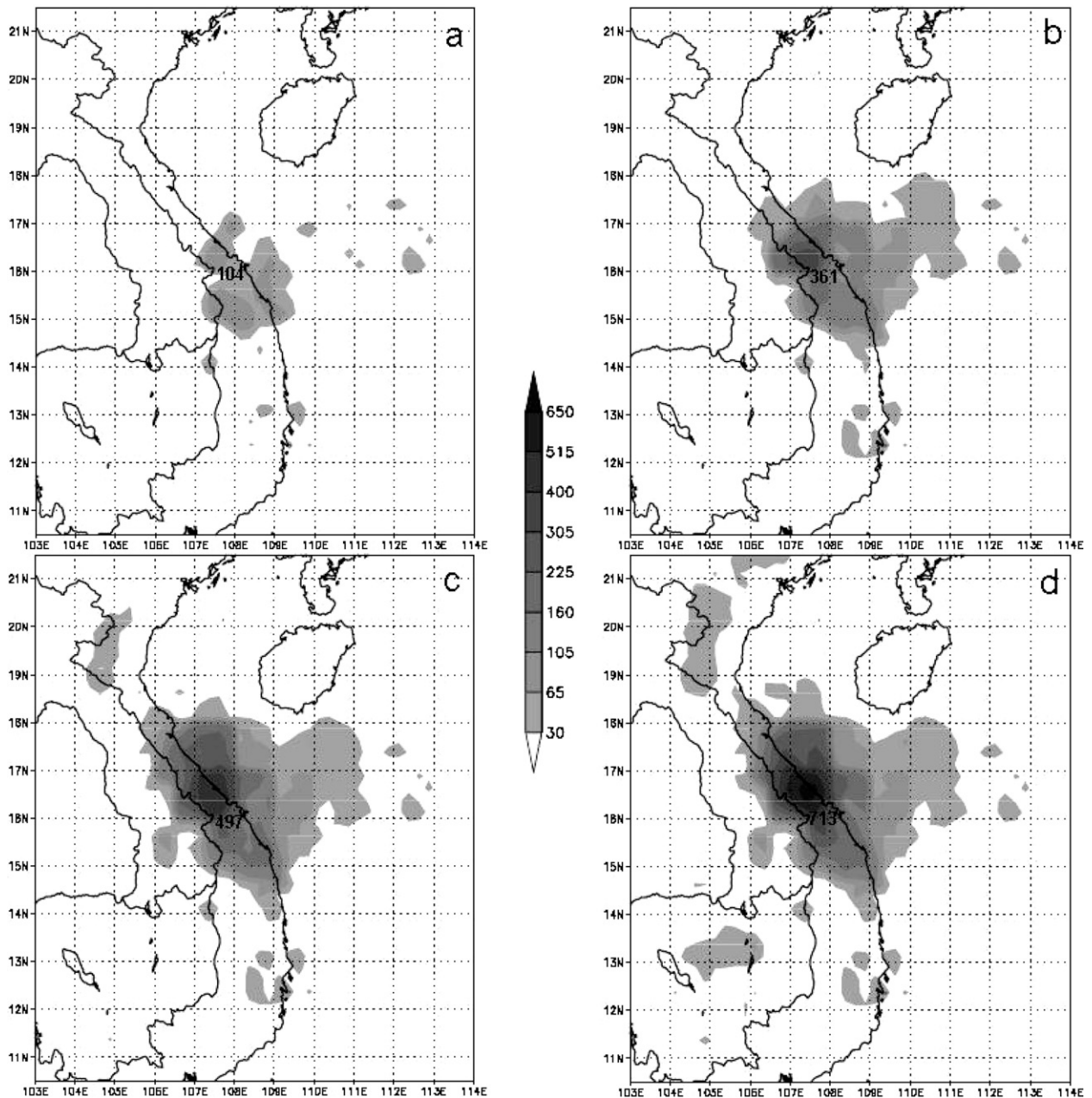
FIG. 6. As in Fig. 5, but for TRMM data.

trigger function but is also dependent on the method used to compute updraft velocity and closure assumption.

When all modifications are used, the 48-h TASR shows very impressive results as given in Fig. 7d (the 12-, 24-, and 36-h TASR are not shown but manifest much better than previous cases). That is, the maximum 48-h TASR comes to 673 mm (93% of the AOR) and the northward expansion of the heavy rainfall region is very well captured. This case gives the best results in

comparison with the observed and TRMM data. The rainfall evolution follows very close to TRMM data (Table 2) and the simulated rainfall region in the southwest corner of the domain is not found. With the foregoing results the new trigger function indicates its reliability in reproducing the distribution and evolution of the TASR. Its advantage is that it does not depend on as many empirical coefficients as the original one since it is derived basing on an explicit physical mechanism.
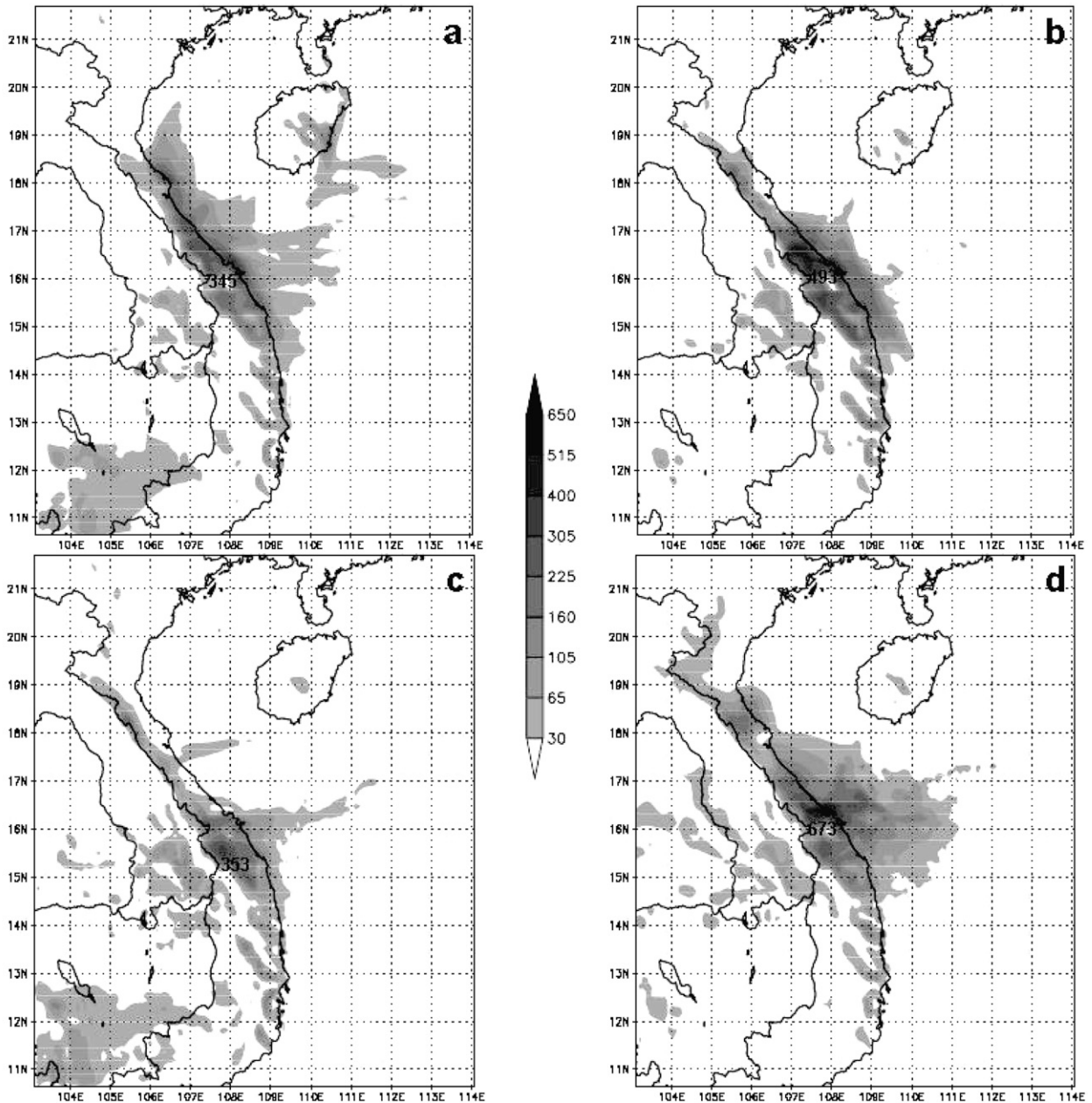
FIG. 7. Horizontal distribution of 48-h TASR (mm) for (a) case I-ori, (b) I-tri, (c) I-cue, and (d) I-all: using the original KF scheme, modified KF trigger function, modified KF updraft velocity and closure assumption, and all modifications, respectively.

c. Resolvable simulated rainfall and the interaction between convection and larger-scale environment

With the event simulations above, the contribution of the 48-h resolvable accumulative simulated rainfall (RASR) is shown in Fig. 8 for cases I-ori, I-tri, I-cue, and I-all. Note that in either case, the RASR locates to the north of Bach Ma Mountain. The original KF CPS associates with the smallest RASR that locates very far

from the mountain (Fig. 8a), meanwhile the modified one gives the largest convective accumulative simulated rainfall (CASR) just to the north of the mountain (not shown) and a concomitant region of larger amount of RASR, which shifts a little bit more northward. This means there is a transition zone between the CASR and RASR regions. Other cases produce much longer bands of larger RASRs, which expand from the windward side of the mountain to the north (Figs. 8b–d). In

TABLE 2. Temporal evolution of the maximum TASR (mm) for four cases.

Case	12 h	24 h	36 h	48 h
I-ori	108	204	294	345
I-tri	120	244	366	493
I-cue	138	293	346	353
I-all	179	347	532	673

addition, while remaining northeast at lower levels in the grid 2 region on both days (Fig. 2), the wind field at upper levels (e.g., 500 mb) rotates southeast to southwest as depicted in Fig. 9 creating a return flow above the northeast winter monsoon.

To qualitatively evaluate the distribution of the 48-h RASR given by four cases, the 48-h accumulative stratiform precipitation is computed using satellite TMI data (see online at http://rain.atmos.colostate.edu/). TMI data consist of only two observations per day, and they also contain missing pixels that may cause a significant underestimation of precipitation when taking average for individual grid boxes. However, the TMI stratiform precipitation shows the best agreement with the RASR given by the modified scheme (not shown).

Accordingly, to show the interaction between convection and the larger-scale environment, the vertical cross sections along line AB in Fig. 8d for the wind vector, convective heating rate, and total condensate mixing ratio are given in Fig. 10 for case I-ori, at 0600, 1200, and 1800 UTC 24 November and at 0000, 0600, and 1200 UTC 25 November 2004. Vertical distributions at 1800 UTC 25 November and 0000 UTC 26 November 2004 (neither shown) look like Fig. 10f. A prominent feature in this case is that convection is weakly activated to the south of Bach Ma Mountain (Figs. 10b–d), causing significant underestimation of the TASR as shown in Fig. 7a. The original scheme produces remarkably wide convective heating cells on the windward side of Bach Ma Mountain where upward motions are strong even though almost no condensate is formed in the return flow at upper levels. This result leads to very small RASR to the north of the mountain as seen in Fig. 8a and shows a weak interaction between convection and its environment.

In the same fashion, the vertical cross sections for case I-all are illustrated in Fig. 11. Vertical distributions at 1800 UTC 25 November and 0000 UTC 26 November 2004 are not shown since they are similar to Fig. 11e. Contrary to case I-ori, the modified KF CPS produces much thinner convective heating cells that frequently appear to the south of Bach Ma Mountain (Figs. 11a–f), leading to much larger TASR as depicted

in Fig. 7d. More interestingly, at 1800 UTC 24 November 2004, a large amount of condensate is found in a deep layer between 5 and 10 km above ground level (AGL), which then moves northward with the return flow, producing a ~200-km-wide band of stratiform cloud on the windward side of the mountain. The band of stratiform cloud is the reason of much larger RASR as mentioned above. A close-up look at Fig. 11 shows that below the wider band of stratiform cloud, between 4.5 and 8 km AGL (associated with alto-stratiform cloud), is a narrower band between 1.5 and 3 km AGL. Between the two bands is a layer of clear environmental air, where upward motions are relative strong. Clearly, the modified KF CPS manifests a much stronger interaction with its larger-scale environment, and reproduces cloud systems that are consistent with our understanding of cloud systems near the southern edge of cold air masses or frontal zones. Thus, the interaction between convection and its environment depends not only on CPS itself but also on the feature of larger-scale circulation. Specifically, the Bach Ma Mountain becomes a barrier to the thin cold air mass and forces it to move upward and finally to enter westerly flows at upper levels, causing the return flow as mentioned. In such situations, local forecasters usually warned of larger amounts of stratiform rainfall associated with stationary fronts.

According to Figs. 10 and 11, the bands of stratiform cloud first fully develop along with strong convection around 0600 UTC (1300 LT) 25 November 2004. That is why some auxiliary vertical sections and soundings are investigated. Zonal-vertical cross sections at point A and B in Fig. 8d for the wind vector and pressure perturbation at 0600 UTC 25 November 2004 are given in Fig. 12 for case I-ori (Figs. 12a,b) and I-all (Figs. 12c,d). In either case, there are strong upward gradients of pressure perturbation in the windward side of the Truong Son Mountains, where convection is strongly activated (not shown). This is a reasonable explanation for the much larger TASR given by the modified KF CPS and illustrates the necessity of taking pressure perturbation into account. There is also a noticeable difference, that is, the modified scheme produces meso highs centered near 2000 m above the MSL far from the mountain to the east, which might lead to the mesoscale descending motion entering the boundary layer and, thus, suppressing the occurrence of convection. The meso low in the boundary layer in Fig. 12d might be caused by the vestige of Typhoon Muifa.

Soundings given by RAMS at point A (Fig. 8d) at this time are represented in Fig. 13 for cases I-ori and I-all. In general, the modified scheme makes the larger-
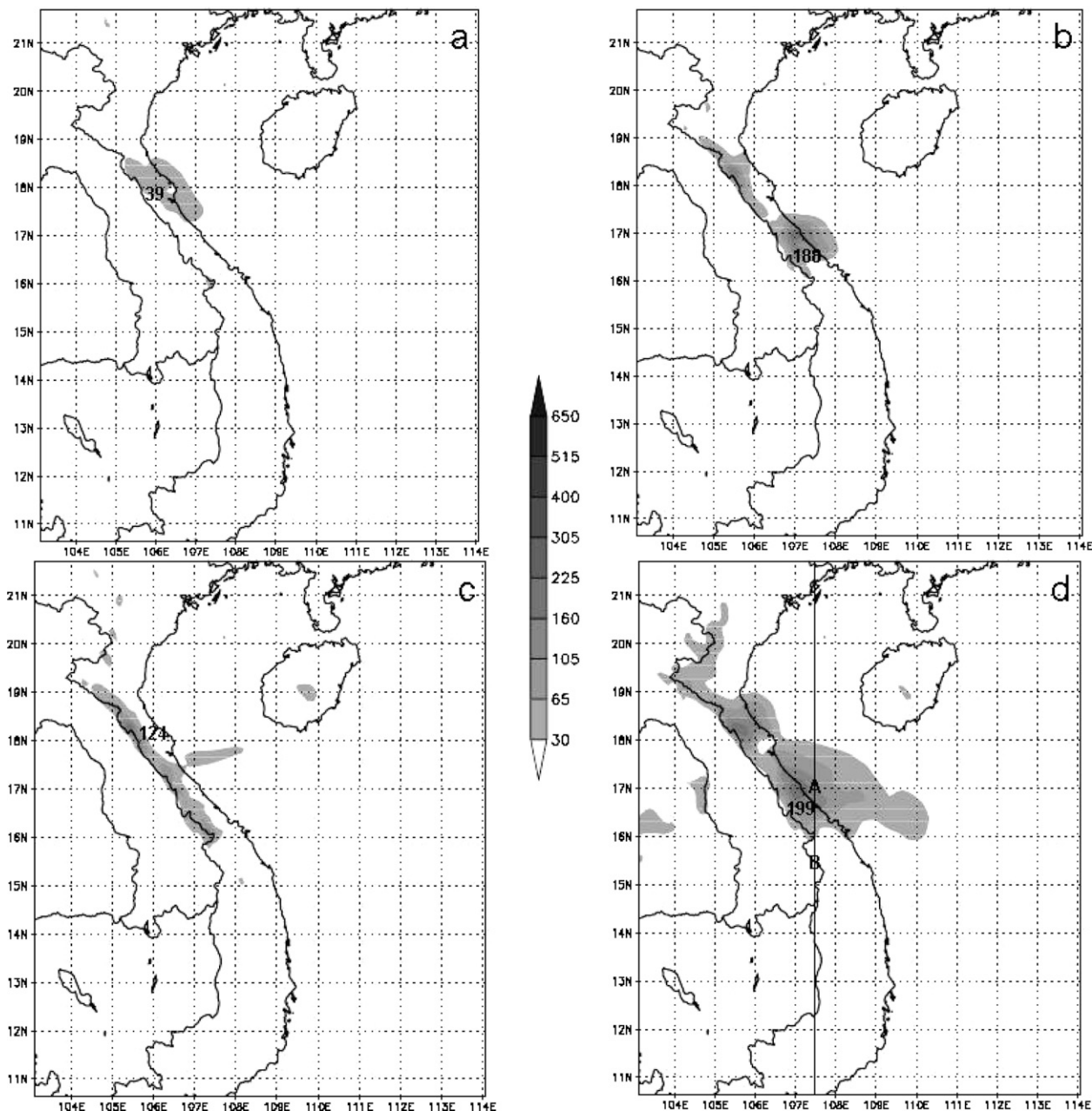
FIG. 8. As in Fig. 7, but for 48-h RASR.

scale environment moister, especially at levels higher than 200 mb. At point A, the modified scheme produces a thin, dry neutral layer above 700 mb, which is associated with the clear environmental air shown in Fig. 11. Meanwhile, the original scheme gives a smooth vertical temperature profile. The explanation for this difference might be that the original scheme makes convection artificially occur more frequently to the north of the Bach Ma Mountain, which smoothes the temperature profile. Neutral and inversion layers were

frequently observed when cold air masses traverse the South China Sea and adjacent regions (Henry and Thompson 1978; Ding and Krishnamurti 1987; Trier et al. 1990). However, in this study, specific soundings are not available so no further discussion is presented.

To the south of the Bach Ma Mountain, Figs. 10 and 11 suggest that convection strongly develops around 0600 UTC (1300 LT) 24 November 2004. Figure 14a illustrates the vertical profile of the updraft velocity at
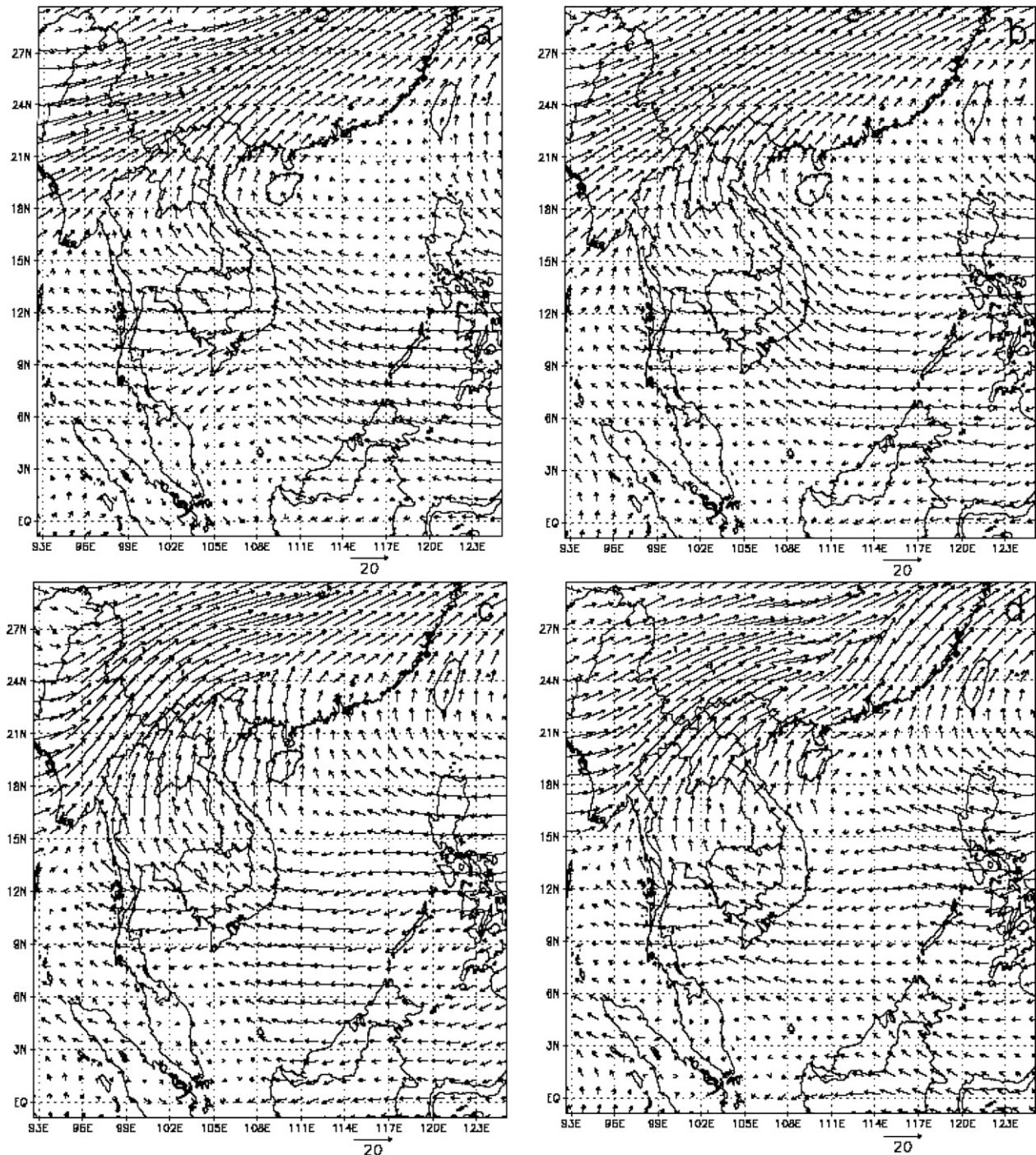
FIG. 9. Wind field over Vietnam and the South China Sea region at 500 mb at (a) 1200 UTC 24 Nov, (b) 0000 UTC 25 Nov, (c) 1200 UTC 25 Nov, and (d) 0000 UTC 26 Nov 2004, grid 1, case I-all: modified KF trigger function, updraft velocity, and closure assumption.

point B (Fig. 8d) at this time. Accordingly, the modified scheme produces taller convective clouds with much stronger updraft velocity in the whole cloud layer, especially at the LCL and near the cloud top. This is the reason why the modified scheme gives a larger convec-

tive precipitation rate and moister environment at the upper levels (not shown). When the first terms (updraft forces) in Eqs. (3) and (7) are computed for each model layer, Fig. 14b shows that the modified scheme generates stronger model-layer updraft energy near the cloud
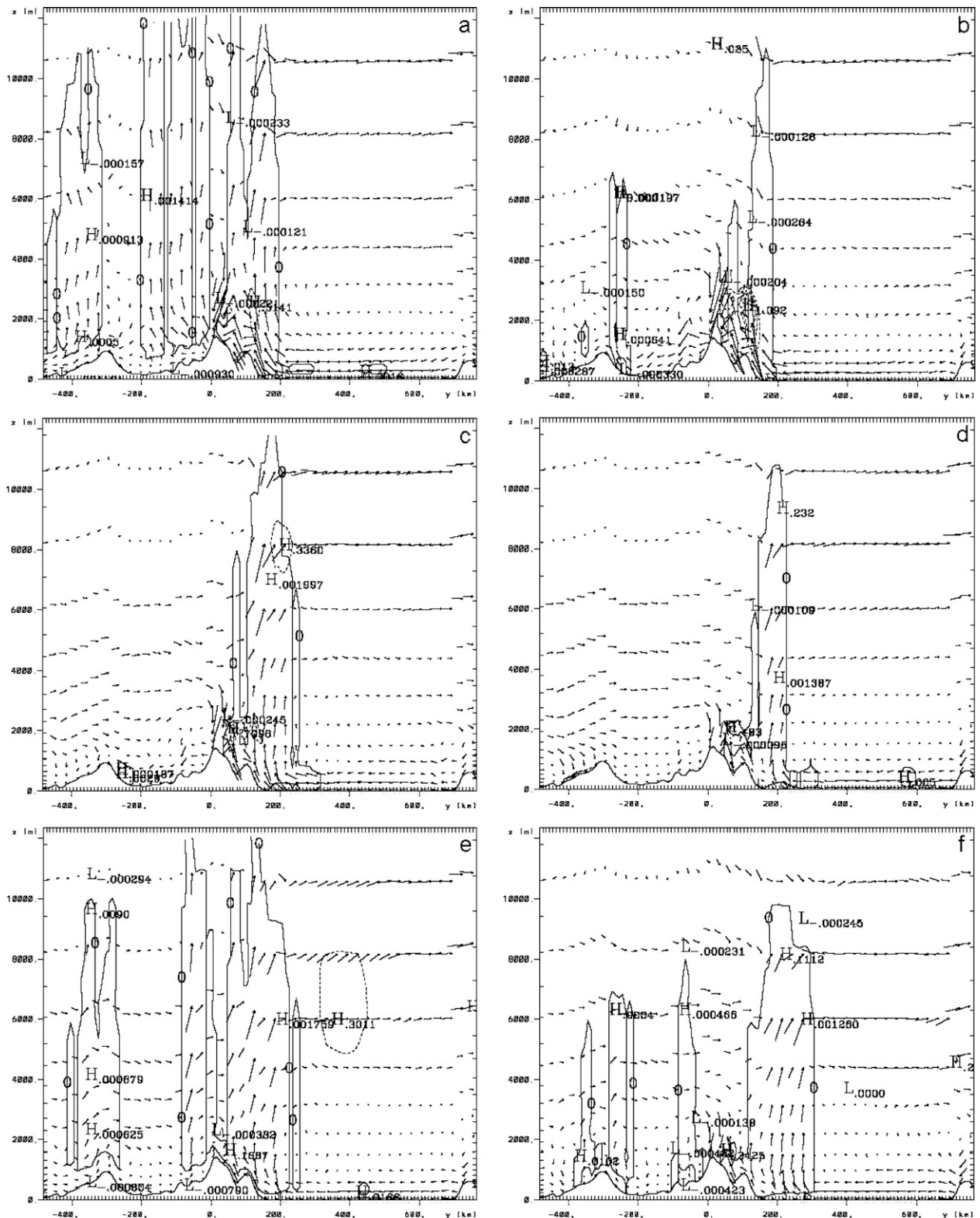
FIG. 10. Vertical cross section along line AB in Fig. 8d for the wind vector, convective heating rate (solid line, contour interval is 2×10^{-3} K s^{-1}), and total condensate mixing ratio (dashed line, contour interval is 25×10^{-2} g kg^{-1}) at (a) 0600, (b) 1200, (c) 1800 UTC 24 Nov and (d) 0000, (e) 0600, and (f) 1200 UTC 25 Nov 2004, case I-ori: original KF scheme.
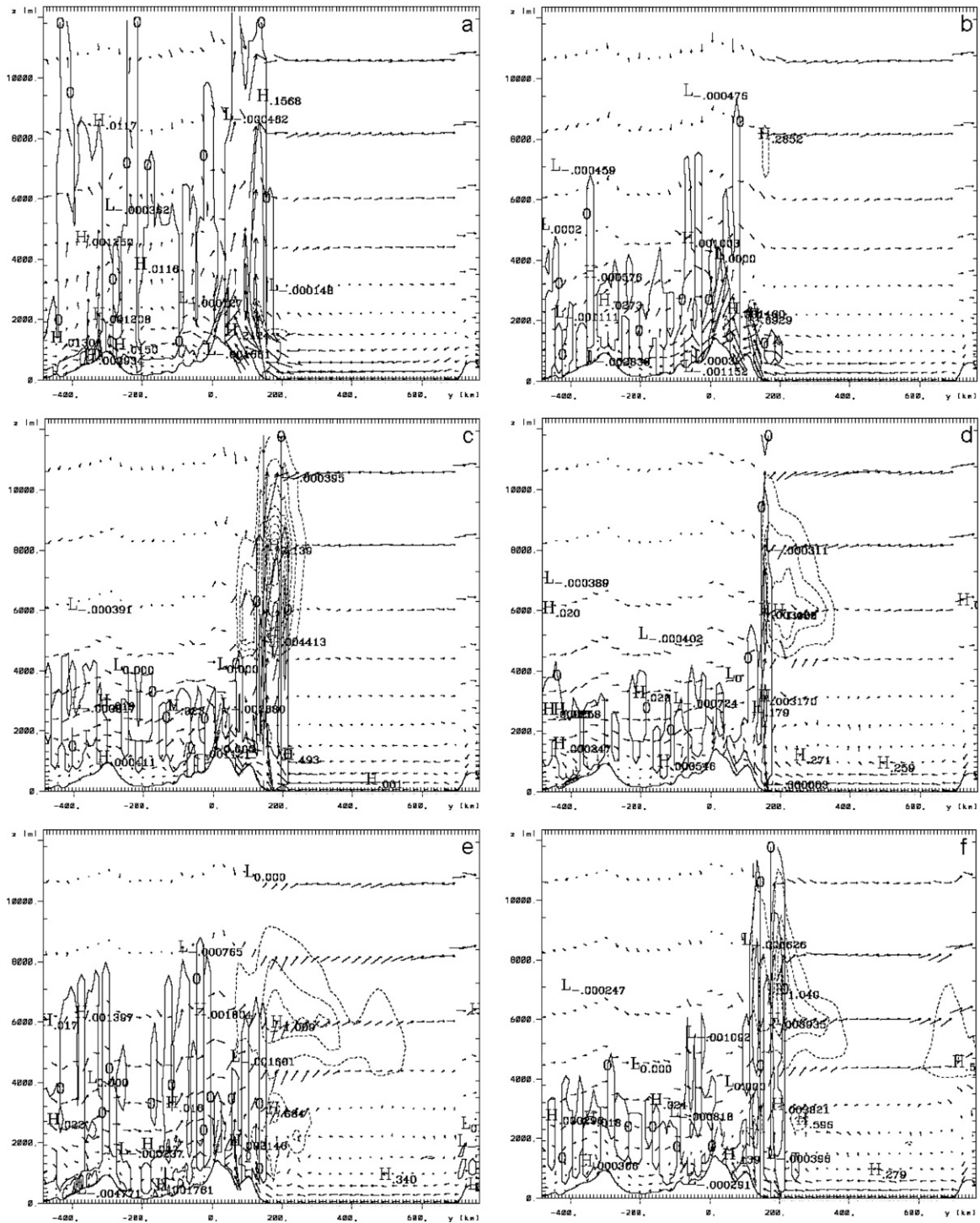
FIG. 11. As in Fig. 10, but for case I-all: modified KF trigger function, updraft velocity, and closure assumption.

top, thereby leading to much stronger updraft velocity as mentioned. Meanwhile, both original and modified schemes give very small updraft energy near the LCL. Thus, in this case the new trigger function creates stronger updraft velocity at the LCL.

d. Inclusion of the advective terms

To clarify, if the inclusion of the advective terms can contribute to the TASR, the on–off coefficient in Eq. (15), equal to a_u, is considered. However, the inclusion
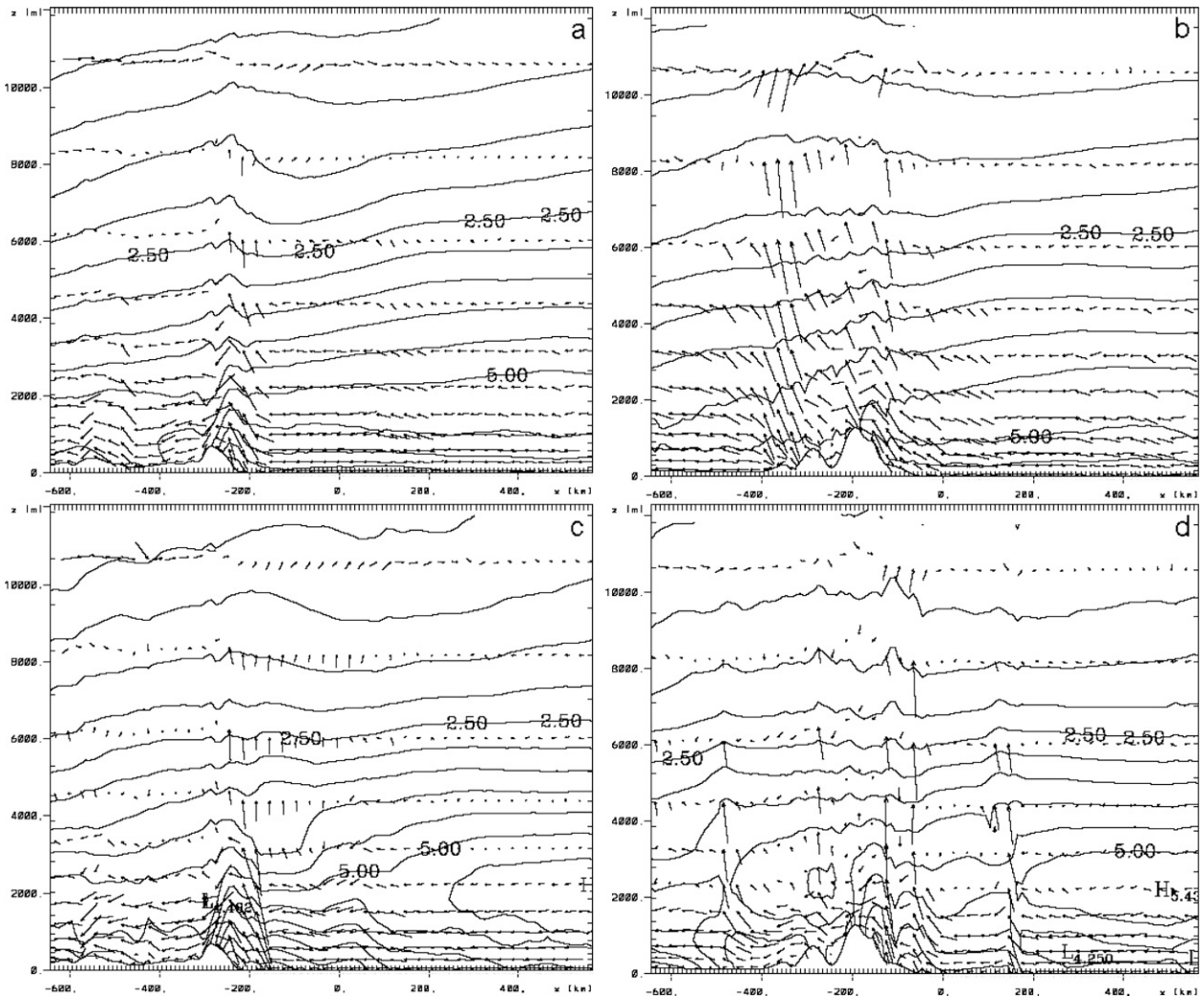
FIG. 12. Zonal–vertical cross section at points A and B in Fig. 8d for the wind vector and pressure perturbation at 0600 UTC 25 Nov 2004, for (a), (b) case I-ori and (c), (d) I-all: using the original KF scheme and all modifications, respectively.

makes almost no change in the TASR (not shown). This means that either the advective terms play almost no role in the formation and development of convective clouds (for this region) or they cannot be parameterized in the CPS as given in section 2 showing that the advective terms contribute to the updraft acceleration with a weight that is much larger than a_u.

5. Summary and concluding remarks

The region of central Vietnam is mountainous with short and steep rivers. Tropical weather systems that originate offshore in the South China Sea are a common occurrence during the transition seasons. The threat of local flash floods is high during these periods and skillful heavy rainfall forecasts are essential. The modified KF CPS, using a new diagnostic equation to compute the updraft velocity, closure assumption, and

trigger function, significantly improves the TASR. The vertical gradient of the Exner function perturbation thus appears to play an important role in the parameterization of convection in regions of complex terrain.

In the present study, the CAPE definition is extended, unlike the traditional definition, to contain a dynamic term which when used with the new equation to compute the updraft velocity, might maintain convection even in an environment of negative buoyancy if the pressure gradient can support convection against the negative buoyancy. When the new trigger function is tested, it shows a promising reliability and the most important advantage is that the new function is developed based on an explicit physical mechanism and fewer empirical coefficients are used.

The simulated precipitation shows that for event simulations, the modified KF CPS gives the best results
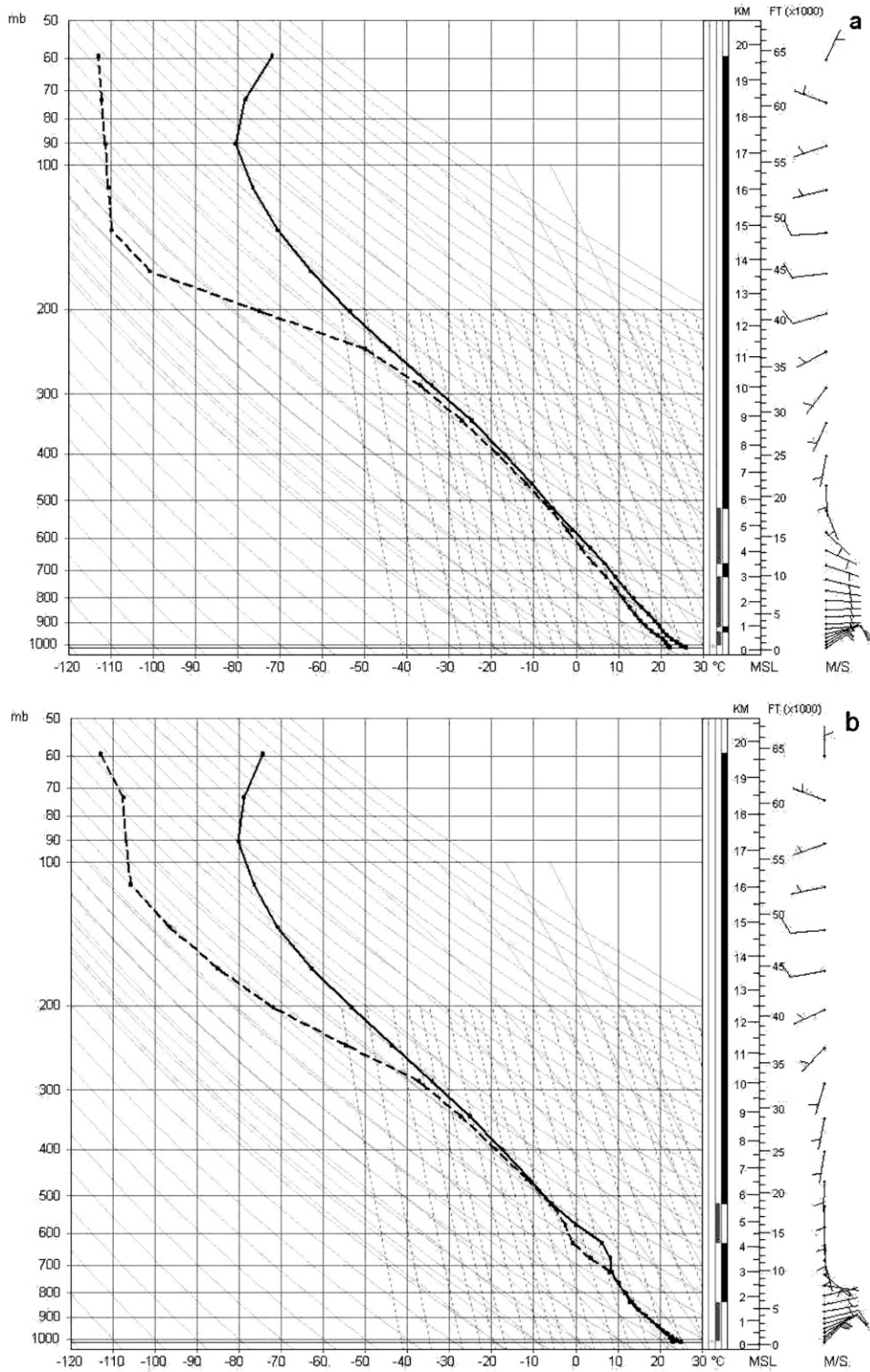
FIG. 13. Sounding given by RAMS at point A in Fig. 8d at 0600 UTC 25 Nov 2004, for (a) case I-ori and (b) I-all: using the original KF scheme and all modifications, respectively.
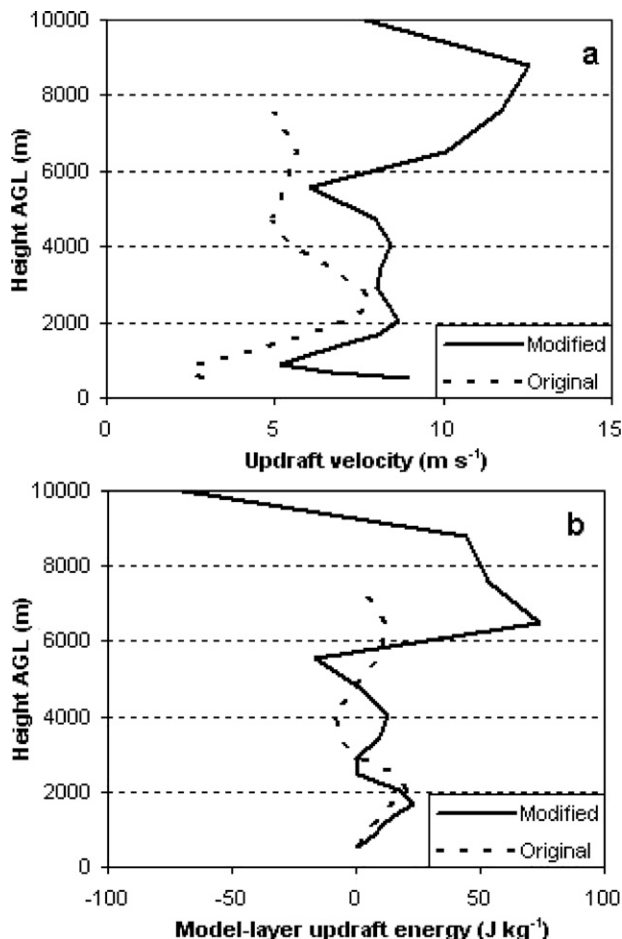
FIG. 14. Vertical profile at point B in Fig. 8d at 0600 UTC 24 Nov 2004 for (a) the updraft velocity and (b) model-layer updraft energy, for case I-ori and I-all: using the original KF scheme (dashed line) and all modifications (solid line), respectively.

in comparison with the observed and TRMM data in both distribution and temporal evolution. By contrast, the original KF CPS gives a significant underestimation of the TASR. In addition, it produces a rainfall region in the southwest corner of the domain, which might be unreasonable. Simulations given by case I-ori, I-tri and I-cue show that where convection occurs is not uniquely decided by the trigger function but depends also on the equation to compute updraft velocity and closure assumption. However, the new trigger function reproduces much larger TASR (case I-tri). These results state that the trigger function and updraft component can become blurred since, on the first hand, convection only occurs if the updraft component produces cloud layers deep enough (Kain 2004). On the other hand, the trigger function determines the updraft velocity at the LCL, which is the lower boundary value for the equation to compute updraft velocity. Therefore, the trigger

function needs to be developed along with other components of the CPS as a whole.

The interaction between convection and larger-scale environment depends not only on CPS itself but on the feature of topography and larger-scale circulation as well. Specifically, the modified KF CPS produces much larger RASR from the windward side of Bach Ma Mountain northward, where the return flow prevails at upper levels. Moreover, it reproduces cloud systems that are consistent with our understanding of cloud systems near the southern edge of cold air masses or cold frontal zones. Thus, convective cells given by the modified KF CPS play the role of a "moist bridge" which brings moisture from lower layers to upper layers and creates bands of stratiform cloud in the return flow.

In general, the modified KF CPS is more effective than the original one in moistening larger-scale environment. In addition, it also produces a dry neutral layer just above 700 mb in the region where the cold air mass dominates at lower levels, which is consistent with observed data given by other studies. While doing this research we realize that our case study contains features similar to the core domain of the NAME (North American Monsoon Experiment) field campaign 2004 (Johnson et al. 2007; Lang et al. 2007; Williams et al. 2007). For example, the Sierra Madre Occidental runs along the Gulf of California also creating a narrow plain where rainfall distributes along the coast with a large mount of stratiform rainfall. Moreover, the wind shear is also different between the northern and southern portion of the domain. Thus, it would be valuable if the present study could be expanded using the NAME unprecedented data. Finally, results of the present study are promising in the sense that an integrated system can be built for flood warning for central Vietnam, where model rainfall forecasts are used for hydrological models.

APPENDIX

The Analytical Relation between Updraft Forces

Since pressure perturbation becomes the source of the modifications, it is reasonable to start with the 3D

steady-state third equation of motion used in RAMS, aiming at finding an expression where pressure (or the Exner function) perturbation is directly taken into account or indirectly accounted for by a relation with another term (buoyancy in this case):

$$\overline{u}\frac{\partial \overline{w}}{\partial x} + \overline{v}\frac{\partial \overline{w}}{\partial y} + \overline{w}\frac{\partial \overline{w}}{\partial z} = g\frac{\theta'}{\theta_0} - \theta_0\frac{\partial \pi'}{\partial z}, \qquad \text{(A1)}$$

where θ and π are the virtual potential temperature and the Exner function, respectively; "0" and the prime denote, respectively, the synoptic-scale variables and the mesoscale deviations from this larger scale (e.g., Pielke 2002). Other symbols are conventional. In RAMS the Exner function is defined by

$$\pi = C_p(p/p_{00})^{R_d/C_p}, \qquad \text{(A2)}$$

where $p_{00} = 1000$ hPa, and an arbitrary synoptic scale (Φ_0) is defined by

$$\Phi_0 = \frac{1}{D_x D_y}\int_x^{x+D_x}\int_y^{y+D_y}\overline{\Phi}\,dx\,dy, \qquad \text{(A3)}$$

where D_x and D_y are much greater than the grid size so that synoptic-scale thermodynamic variables are presumed hydrostatic.

For convenience in deriving the remaining equations, the virtual absolute temperature is used instead of the virtual potential temperature. Using the relation between the specific volume and other thermodynamic variables as in Pielke (2002):

$$\frac{\alpha'}{\alpha_0} \approx \frac{T'}{T_0} - \frac{p'}{p_0} \qquad \text{(A4)}$$

and

$$\frac{\alpha'}{\alpha_0} = \frac{\theta'}{\theta_0} - \frac{C_v}{C_p}\frac{p'}{p_0} \qquad \text{(A5)}$$

one obtains

$$\frac{\theta'}{\theta_0} = \frac{T'}{T_0} - \frac{p'}{p_0}\left(1 - \frac{C_v}{C_p}\right), \qquad \text{(A6)}$$

where C_v, C_p, and α are the heat capacities at constant volume and constant pressure, and the specific volume, respectively. Substitution of Eq. (A6) into Eq. (A1) yields

$$\overline{w}\frac{\partial \overline{w}}{\partial z} = g\left[\frac{T'}{T_0} - \frac{p'}{p_0}\left(1 - \frac{C_v}{C_p}\right)\right] - \theta_0\frac{\partial \pi'}{\partial z} + \text{ADV}, \qquad \text{(A7)}$$

where $\text{ADV} = -\overline{u}(\partial \overline{w}/\partial x) - \overline{v}(\partial \overline{w}/\partial y)$ is the advection of the vertical velocity due to the grid-scale horizontal velocity. According to the definition of the grid-scale average and the mesoscale fluctuation (Pielke 2002), Eq. (A7) can be rewritten as

$$(a_u w_u + a_d w_d)\frac{\partial(a_u w_u + a_d w_d)}{\partial z} = g\left[\frac{a_u(T_u - T_0)}{T_0} - \frac{a_u(p_u - p_0)}{p_0}\left(1 - \frac{C_v}{C_p}\right)\right]$$
$$+ g\left[\frac{a_d(T_d - T_0)}{T_0} - \frac{a_d(p_d - p_0)}{p_0}\left(1 - \frac{C_v}{C_p}\right)\right]$$
$$- \theta_0\frac{\partial a_u(\pi_u - \pi_0)}{\partial z} - \theta_0\frac{\partial a_d(\pi_d - \pi_0)}{\partial z} + \text{ADV}, \qquad \text{(A8)}$$

where a_u and a_d are the updraft and out-of-updraft fractional areas, respectively, and where the sum $a_u + a_d$ is equal to 1 and represents the total area of the grid cell. The subscript "u" denotes the updraft and "d" denotes the out-of-updraft properties. In manipulating Eq. (A8), the relations $\Phi' = \overline{\Phi} - \Phi_0$ and $\overline{\Phi} = a_u\Phi_u + a_d\Phi_d$ are used. The first and third terms on the right-hand side of Eq. (A8) are the buoyant force and the force associated with the vertical gradient of the Exner function perturbation, equivalent to pressure perturbation, which occurs within the updrafts (updraft forces). The second and fourth terms are the buoyant force and the force associated with the vertical gradient of the Exner function perturbation, which occurs out of the updrafts (environment forces). The left-hand side of Eq. (A8) can be rewritten as

$$(a_u w_u + a_d w_d)\frac{\partial(a_u w_u + a_d w_d)}{\partial z} = a_u w_u\frac{\partial a_u w_u}{\partial z} + a_d w_d\frac{\partial a_u w_u}{\partial z} + a_u w_u\frac{\partial a_d w_d}{\partial z} + a_d w_d\frac{\partial a_d w_d}{\partial z}. \qquad \text{(A9)}$$

The first term on the right-hand side of Eq. (A9) describes the vertical change rate of the updraft kinetic energy and the fourth term describes the vertical change rate of the out-of-updraft kinetic energy. Physi-

cally, these vertical change rates of kinetic energy are caused by the updraft and environment forces. To clarify the physical meaning of the second and third terms we consider the steady-state form of governing Eqs. (29) and (30) in Lappen and Randall (2001):

$$\rho A_u w_u \frac{\partial h_u}{\partial z} = E A_g (h_d - h_u) + \rho (S_h)_u A_u \tag{A10}$$

and

$$\rho A_d w_d \frac{\partial h_d}{\partial z} = D A_g (h_u - h_d) + \rho (S_h)_d A_d, \tag{A11}$$

where A_g, A_u, and A_d are the grid cell area and areas occupied by the updraft and the environment. Here E, D, and S_h are conceptually defined as the entrainment and detrainment rates, and the source term, respectively, and h is an arbitrary intensive variable. If dividing both sides of the equations by ρ and A_g, and defining $h_u = a_u w_u$ and $h_d = a_d w_d$:

$$a_u w_u \frac{\partial a_u w_u}{\partial z} = \frac{E}{\rho}(a_d w_d - a_u w_u) + (S_h)_u a_u \tag{A12}$$

and

$$a_d w_d \frac{\partial a_d w_d}{\partial z} = \frac{D}{\rho}(a_u w_u - a_d w_d) + (S_h)_d a_d. \tag{A13}$$

Combining Eqs. (A12) and (A13) and comparing them with Eqs. (A8) and (A9), the second and third terms on the right-hand side of Eq. (A9) are implicitly defined as the entrainment and detrainment terms. If the entrainment and detrainment are simultaneous processes affecting the updraft and its environment, then the definition for the entrainment or detrainment depends on the sign of $\partial(a_u w_u a_d w_d)/\partial z$. The final state of the vertical velocities primarily depends on the updraft and environment forces since they are external forcings. Equation (A8) can then be decomposed into two equations one for the downdraft and one for the updraft. The latter can be written as

$$a_u w_u \frac{\partial a_u w_u}{\partial z} = g\left[\frac{a_u(T_u - T_0)}{T_0} - \frac{a_u(p_u - p_0)}{p_0}\left(1 - \frac{C_v}{C_p}\right)\right] - \theta_0 \frac{\partial a_u(\pi_u - \pi_0)}{\partial z} + \text{ADV} + \text{Ent}, \tag{A14}$$

where Ent denotes the entrainment already accounted for in the original KF CPS. Next, if it is assumed that the updraft parcels immediately experience the grid-scale pressure (Anthes 1977) then the above equation can be rewritten as

$$\frac{1}{2}\frac{\partial a_u^2 w_u^2}{\partial z} = g\left[\frac{a_u(T_u - T_0)}{T_0} - \frac{a_u(\bar{p} - p_0)}{p_0}\left(1 - \frac{C_v}{C_p}\right)\right] - \theta_0 \frac{\partial a_u(\bar{\pi} - \pi_0)}{\partial z} + \text{ADV} + \text{Ent}. \tag{A15}$$

Physically, the updrafts embedded in a model grid box having positive advection of the grid-scale vertical velocity are accelerated. Unfortunately, the contribution to the updraft velocity of the advective terms is not quantitatively known yet. To clarify its role an on–off coefficient is added to Eq. (A15):

$$\frac{1}{2}\frac{d a_u^2 w_u^2}{dz} = g\left[\frac{a_u(T_u - T_0)}{T_0} - \frac{a_u(\bar{p} - p_0)}{p_0}\left(1 - \frac{C_v}{C_p}\right)\right] - \theta_0 \frac{\partial a_u(\bar{\pi} - \pi_0)}{\partial z} + C_{\text{adj}}.\text{ADV} + \text{Ent}, \tag{A16}$$

where the on–off coefficient (C_{adj}) is equal to a_u (or 0) to (or not to) formalistically account for the contribution of the advective terms to acceleration or deceleration of the updraft velocity. Note that Eq. (A16) does not contain the term to account for the effect of drag since the third equation of motion also does not contain this term. However, this term can be taken into account using an empirical expression as the original scheme. There are two major differences between Eqs. (A16) and (3). First, the vertical gradient of the Exner function perturbation, equivalent to the pressure perturbation, is explicitly taken into the equation for the updraft velocity. Second, the horizontal advection of vertical velocity is taken into account and its effect on the updraft acceleration is parameterized.

Unfortunately, when Eq. (A16) is directly applied two difficulties arise: first, the updraft area cannot be computed exactly (Kain 2004), and this might lead to inaccurate updraft velocity since its power is not the same on the both sides of the equation; second, the updraft buoyancy is not consistent with the CAPE definition, which is used for the closure assumption. However, the ratio (PDB) between the second (plus the third term if the advective terms are taken into account) and first terms on the right-hand side of Eq. (A16) can be computed, assuming that the updraft area is constant with height:

$$\text{PDB} = -\frac{\theta_0 \frac{\partial(\bar{\pi} - \pi_0)}{\partial z}}{g\left[\frac{T_u - T_0}{T_0} - \frac{\bar{p} - p_0}{p_0}\left(1 - \frac{C_v}{C_p}\right)\right]}. \tag{A17}$$

Note that PDB can be computed using Eq. (A8), however, Eq. (A16) is derived to show if it can analytically describe physical processes associated with updrafts. If so, using its consequence is reliable.

Finally, it is worth noting that steady-state Eq. (A1) is used because of two reasons: the Kain–Fritsch scheme implements the steady-state updraft model and Eq. (A16) is used to compute PDB instead of updraft velocity directly. This is fine for consistency because steady-state updraft buoyancy requires that the perturbation pressure gradient force is in a steady state. Otherwise, if nonsteady-state updraft forces are required, it is expected that we have to face very difficult, if not impossible, problems in mathematics, physical understanding of convective clouds (e.g., cloud model), and computation. Therefore, in the present study, PDB is assumed to be in a steady state in very short times between CPS activations.

REFERENCES

Anthes, R. A., 1977: A cumulus parameterization scheme utilizing a one-dimensional cloud model. *Mon. Wea. Rev.,* **105,** 270–286.

Arakawa, A., and W. H. Schubert, 1974: Interaction of a cumulus cloud ensemble with the large-scale environment. Part I. *J. Atmos. Sci.,* **31,** 674–701.

Cai, H., and R. M. Wakimoto, 2001: Retrieved pressure field and its influence on the propagation of a supercell thunderstorm. *Mon. Wea. Rev.,* **129,** 2695–2713.

Castro, C. L., 2005: Investigation of the summer climate of North America: A regional atmospheric modeling study. Ph.D. dissertation, Colorado State University, 210 pp.

Chen, S.-H., and Y.-L. Lin, 2005: Effects of moist Froude number and CAPE on a conditionally unstable flow over a mesoscale mountain ridge. *J. Atmos. Sci.,* **62,** 331–350.

Chu, C.-M., and Y.-L. Lin, 2000: Effects of orography on the generation and propagation of mesoscale convective systems in a two-dimensional conditionally unstable flow. *J. Atmos. Sci.,* **57,** 3817–3837.

Cohen, C., 2002: A comparison of cumulus parameterizations in idealized sea-breeze simulations. *Mon. Wea. Rev.,* **130,** 2554–2571.

Cotton, W. R., and Coauthors, 2003: RAMS 2001: Current status and future directions. *Meteor. Atmos. Phys.,* **82,** 5–29.

Ding, Y., and T. N. Krishnamurti, 1987: Heat budget of the Siberian high and the winter monsoon. *Mon. Wea. Rev.,* **115,** 2428–2449.

Donner, L. J., 1993: A cumulus parameterization including mass fluxes, vertical momentum dynamics, and mesoscale effects. *J. Atmos. Sci.,* **50,** 889–906.

Doyle, J. D., and D. R. Durran, 2002: The dynamics of mountain-wave-induced rotors. *J. Atmos. Sci.,* **59,** 186–201.

Finley, C. A., W. R. Cotton, and R. A. Pielke Sr., 2001: Numerical simulation of tornadogenesis in a high-precipitation supercell. Part I: Storm evolution and transition into a bow echo. *J. Atmos. Sci.,* **58,** 1597–1629.

Frank, W. M., and C. Cohen, 1985: Properties of tropical cloud ensembles estimated using a cloud model and an observed updraft population. *J. Atmos. Sci.,* **42,** 1911–1928.

Fritsch, J. M., and C. F. Chappell, 1980: Numerical prediction of convectively driven mesoscale pressure systems. Part I: Convective parameterization. *J. Atmos. Sci.,* **37,** 1722–1733.

Grell, G. A., and Y.-H. Kuo, 1991: Semiprognostic tests of cumulus parameterization schemes in the middle latitudes. *Mon. Wea. Rev.,* **119,** 5–31.

Henry, W. K., and A. H. Thompson, 1978: On "return flow" in winter over the East China Sea. *Mon. Wea. Rev.,* **106,** 947–953.

Hong, S. Y., and H. L. Pan, 1998: Convective trigger function for a mass-flux cumulus parameterization scheme. *Mon. Wea. Rev.,* **126,** 2599–2620.

Johnson, R. H., P. E. Ciesielski, B. D. McNoldy, P. J. Rogers, and R. K. Taft, 2007: Multiscale variability of the flow during the North American Monsoon Experiment. *J. Climate,* **20,** 1628–1648.

Kain, J. S., 2004: The Kain–Fritsch convective parameterization scheme: An update. *J. Appl. Meteor.,* **43,** 170–181.

——, and J. M. Fritsch, 1990: A one-dimensional entraining/detraining plume model and its application in convective parameterization. *J. Atmos. Sci.,* **47,** 2784–2802.

——, and ——, 1993: Convective parameterization for mesoscale models: The Kain–Fritsch scheme. *The Representation of Cumulus Convection in Numerical Models, Meteor. Monogr.,* No. 24, Amer. Meteor. Soc., 165–170.

——, M. E. Baldwin, and S. J. Weiss, 2003: Parameterized updraft mass flux as a predictor of convective intensity. *Wea. Forecasting,* **18,** 106–116.

Kalnay, E., and Coauthors, 1996: The NCEP/NCAR 40-Year Reanalysis Project. *Bull. Amer. Meteor. Soc.,* **77,** 437–471.

Klemp, J. B., and R. B. Wilhelmson, 1978a: The simulation of three-dimensional convective storm dynamics. *J. Atmos. Sci.,* **35,** 1070–1096.

——, and ——, 1978b: Simulations of right- and left-moving storms produced through storm splitting. *J. Atmos. Sci.,* **35,** 1097–1110.

Kuo, H. L., 1974: Further studies of the parameterization of the influence of cumulus convection on large scale flow. *J. Atmos. Sci.,* **31,** 1232–1240.

Lang, T. J., D. A. Ahijevych, S. W. Nesbitt, R. E. Carbone, S. A. Rutledge, and R. Cifelli, 2007: Radar-observed characteristics of precipitating systems during NAME 2004. *J. Climate,* **20,** 1713–1733.

Lappen, C.-L., and D. A. Randall, 2001: Toward a unified parameterization of the boundary layer and moist convection. Part I: A new type of mass-flux model. *J. Atmos. Sci.,* **58,** 2021–2036.

Lin, Y.-L., R. D. Farley, and H. D. Orville, 1983: Bulk parameterization of the snow field in a cloud model. *J. Climate Appl. Meteor.,* **22,** 1065–1092.

Mapes, B. E., 2000: Convective inhibition, subgrid-scale triggering energy, and stratiform instability in a toy tropical wave model. *J. Atmos. Sci.,* **57,** 1515–1535.

Pielke, R. A., Sr., 2002: *Mesoscale Meteorological Modeling.* 2nd ed. Academic Press, 676 pp.

——, and Coauthors, 1992: A comprehensive meteorological modeling system RAMS. *Meteor. Atmos. Phys.,* **49,** 69–91.

Raymond, D. J., and A. M. Blyth, 1986: A stochastic mixing model for nonprecipitating cumulus clouds. *J. Atmos. Sci.,* **43,** 2708–2718.

Reynolds, R. W., N. A. Rayner, T. M. Smith, D. C. Stokes, and W. Wang, 2002: An improved in situ and satellite SST analysis for climate. *J. Climate.,* **15,** 1609–1625.

Rogers, R. F., and J. M. Fritsch, 1996: A general framework for convective trigger functions. *Mon. Wea. Rev.,* **124,** 2438–2452.

Rutledge, S. A., and P. V. Hobbs, 1984: The mesoscale and microscale structure and organization of clouds and precipitation in midlatitude cyclone. XII: A diagnostic modeling study of precipitation development in narrow cold-frontal rainbands. *J. Atmos. Sci.,* **41,** 2949–2972.

Tiedtke, M., 1989: A comprehensive mass flux scheme for cumulus parameterization in a large-scale model. *Mon. Wea. Rev.,* **117,** 1779–1800.

Trier, S. B., D. B. Parsons, and T. J. Matejka, 1990: Observations of a subtropical cold front in a region of complex terrain. *Mon. Wea. Rev.,* **118,** 2449–2470.

Walko, R. L., W. R. Cotton, M. P. Meyers, and J. Y. Harrington, 1995: New RAMS cloud microphysics parameterization. Part I: The single moment scheme. *Atmos. Res.,* **38,** 29–62.

Williams, C. R., A. B. White, K. S. Gage, and F. M. Ralph, 2007: Vertical structure of precipitation and related microphysics observed by NOAA profilers and TRMM during NAME 2004. *J. Climate,* **20,** 1693–1712.

Xu, K.-M., and D. A. Randall, 2001: Updraft and downdraft statistics of simulated tropical and midlatitude cumulus convection. *J. Atmos. Sci.,* **58,** 1630–1649.

Yanai, M., and R. H. Johnson, 1993: Impacts of cumulus convection on thermodynamic fields. *The Representation of Cumulus Convection in Numerical Models, Meteor. Monogr.,* No. 46, Amer. Meteor. Soc., 39–62.